TUDelft

Delft University of Technology

Competing magnetic interactions, structure and magnetocaloric effect in $Mn_3Sn_{1-x}Zn_xC$ antiperovskite carbides

Kiecana, A.; Schaefers, W.; Thijs, M.; Dankelman, R.; Ojiyed, H.; Batashev, I.; Zhang, F.; van Dijk, N. H.; Brück, E.

Competing magnetic interactions, structure and magnetocaloric effect in Mn$_3$Sn$_{1-x}$Zn$_x$C antiperovskite carbides

A. Kiecana [a,*], W. Schaefers [a], M. Thijs [a], R. Dankelman [a], H. Ojiyed [a], I. Batashev [b], F. Zhang [a], N.H. van Dijk [a], E. Brück [a]

[a] *Fundamental Aspects of Materials and Energy Group, Department of Radiation Science and Technology, Faculty of Applied Sciences, Delft University of Technology, Mekelweg 15, 2629JB Delft, the Netherlands*
[b] *Radboud University, Institute for Molecules and Materials, Heyendaalseweg 135, 6525 AJ Nijmegen, the Netherlands*

A B S T R A C T

Structural, magnetic and magnetocaloric properties of Mn$_3$Sn$_{1-x}$Zn$_x$C antiperovskite carbides have been studied. With increasing Zn content the first-order magnetic transition (FOMT) is weakened. The Curie temperature (T_C) reduces first from 273 to 197 K and when $x > 0.3$, T_C increases, reaching its maximum of 430 K for $x = 1.0$. An increase in T_C is accompanied by pronounced changes in magnetic behaviour and a significant rise in magnetization from 21.82(4) to 76.2(2) Am^{2}kg^{-1} for $x = 0.8$ in the maximum applied magnetic field of 5 T. Neutron powder diffraction (NPD) was employed to study the magnetic structure of Mn$_3$Sn$_{1-x}$Zn$_x$C compounds. The refinement of the NPD data for $x = 0.3$ revealed a magnetic structure with propagation vector **k** = (½,½,0) with a decrease in the canted antiferromagnetic (AFM) moment, which results in a reduction of the negative volume change at the magnetic transition and a decrease in the magnetocaloric effect (MCE). For $x = 0.4$, the magnetic structure is described by a propagation vector **k** = (½,½,½) for the AFM moment which dominates at low temperature, with the presence of a minor ferromagnetic (FM) component with a **k** = (0, 0, 0) propagation vector, which confirms the presence of the ferrimagnetic (FiM) state. For a higher Zn content ($x = 0.6$), the magnetic moment originates mainly from the FM component found on three independent Mn positions and an additional AFM moment oriented in the *a-b* plane. The results presented confirm the presence of competing AFM-FM interactions in Mn$_3$Sn$_{1-x}$Zn$_x$C antiperovskite carbides.

1. Introduction

The severe impact of traditional compressor-based cooling technologies has pointed the research interest towards seeking alternative cooling systems. Magnetic refrigeration, which utilizes the magnetocaloric effect (MCE), has attracted broad attention due to a number of advantages over traditional compressor-based technologies [1–6]. Magnetocaloric materials (MCM) exhibiting a first-order magnetic phase transition (FOMT) attract particular attention since they provide a large magnetic entropy change ($|\Delta S_m|$), which reflects their cooling capacity. On the other hand, the FOMT is usually associated with a large thermal hysteresis (ΔT_{hys}), which is an obstacle for the practical application of these compounds. Therefore, systems showing a reversible MCE and exhibiting a second-order magnetic transition (SOMT) appear interesting, though their $|\Delta S_m|$ is significantly lower compared to the FOMT

compounds. Various materials exhibiting a SOMT have been studied in terms of their magnetocaloric effect, e.g.: RE$_6$Co$_2$Ga (RE = Ho, Dy, Gd) [7], (Gd$_{1-x}$RE$_x$)$_5$Si$_4$ (RE = Dy, Ho) [8], Mn$_5$PB$_2$ [9], RECo$_{12}$B$_6$ (RE = Ce, Pr, Nd) [10], RENiGa$_2$ [6], RE$_2$Cr$_2$C$_3$ (RE = Er, Ho, Dy) [11].

Mn-based antiperovskites Mn$_3AX$ (A = metal or semiconductor; X = C, N) display a broad variety of interesting phenomena such as giant magnetoresistance (GMR) [12,13], superconductivity [14], magnetovolume effect (MVE) [15,16], piezomagnetic effect [17,18], barocaloric effect [19] and magnetocaloric effect [20–22]. Unlike their perovskite analogues, antiperovskites show metallic behaviour, a good thermal conductivity and a high mechanical stability. In addition, Mn–based alloys consist of abundant, relatively innocuous and inexpensive elements, which enable their practical application in magnetic cooling systems. A particularly large MCE has been recently found in Mn$_3$SnC [22,23] and Mn$_3$GaC [20,24]. The Mn$_3$SnC compound shows a sharp
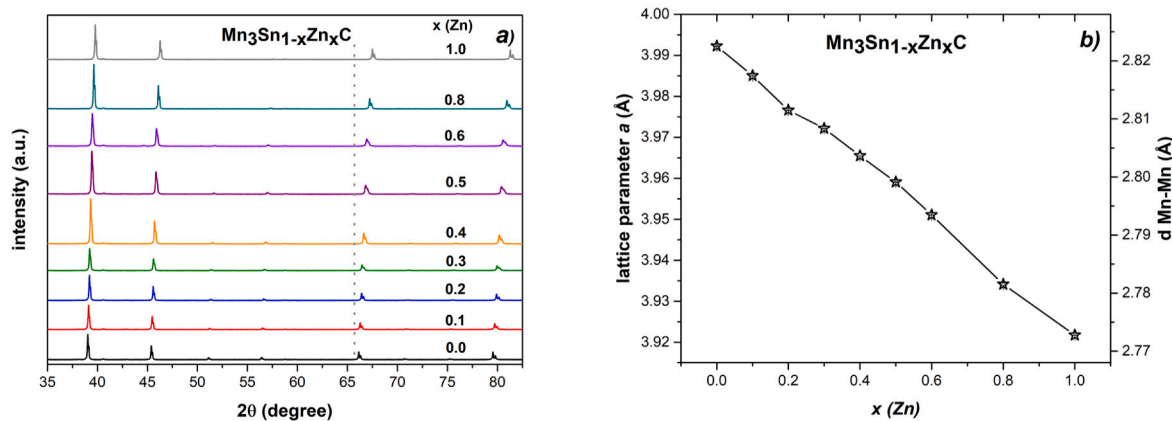
Fig. 1. a) stacked xrd patterns measured at 298 K, b) composition dependence of the lattice parameter *a* and the nearest Mn-Mn distance in $Mn_3Sn_{1-x}Zn_xC$ compounds measured at 298 K. The error bars are smaller than the size of the marker.

and non-hysteretic FOMT from the low-temperature ferrimagnetic (FiM) ordered state consisting of antiferromagnetic (AFM) and ferromagnetic (FM) sublattices, to a high-temperature paramagnetic (PM) state, with $T_C \approx 278$ K [21,22,25]. In another antiperovskite compound – Mn_3ZnC, a transition from a non-collinear FiM state to a FM state ($T_N \approx 233$ K) is followed by a FM-PM transition ($T_C \approx 420$ K) [26,27]. Recent studies deploying ab-initio methods and Monte Carlo (MC) simulations revealed a great potential of the $Mn_3(Sn,Zn)C$ system for the purposes of magnetic refrigeration [26]. Since the systematic investigation of MCE in the $Mn_3Sn_{1-x}Zn_xC$ system was thus far not reported, our main objective was a detailed study on the magnetism, structure and MCE in these compounds using experimental techniques and DFT calculations.

2. Experimental details

Polycrystalline $Mn_3Sn_{1-x}Zn_xC$ ($0.0 \leq x \leq 1.0$) compounds were prepared from Mn (99.7%), Sn (99.9%), Zn (99.9%) and C (99.9%) powders. Stoichiometric proportions of starting materials were thoroughly mixed, pressed into pellets and subsequently sealed in quartz tubes under 200 mbar Ar atmosphere. To compensate for C losses during the annealing process, 10 wt.% extra graphite was added. Since the boiling point of Zn is relatively low (1180 K), significant Zn losses were observed in Zn-rich compounds. Therefore, extra Zn was added to compounds of $x \geq 0.4$ to compensate for metal losses. As-prepared samples were annealed at 1023 K for 120 h and subsequently oven-cooled.

The X-ray diffraction patterns were collected employing a PANalytical X-pert Pro diffractometer using Cu-K$_\alpha$ radiation ($\lambda = 1.54$ Å) equipped with an Anton Paar TTK450 low-temperature chamber. Rietveld refinement implemented in the Fullprof software was used for indexing and lattice constant calculations [28,29]. Neutron powder diffraction (NPD) data were collected at various temperatures in the magnetic and PM state (4 to 475 K), using the neutron powder diffraction instrument PEARL ($\lambda = 1.67$ Å) at the Reactor Institute Delft, the Netherlands. The Rietveld refinement using Fullprof program has been used to elucidate the magnetic structure and magnetic moments. In the refinement, coherent neutron scattering lengths of -0.3730, 0.6225, 0.5680, 0.6646 ($\times 10^{-12}$ cm) were used for Mn, Sn, Zn, C, respectively. Superconducting quantum interference devices (SQUID) MPMS-XL and MPMS-5S magnetometers using the reciprocating sample option mode (RSO) were employed to collect the magnetization data, in the temperature range of 5 to 370 K with a constant sweep rate of 2 K/min and in applied magnetic fields up to 5 T. High-temperature magnetic measurements were performed utilizing a Vibrating Sample Magnetometer (VSM) implemented in the Quantum Design VersaLab.

Density of States (DOS) calculations were performed for $Mn_3Sn_{1-x}Zn_xC$ ($0 \leq x \leq 1.0$) in the framework of density functional

theory utilizing the Vienna Ab Initio simulation package (VASP) [30,31] in the projector augmented-wave (PAW) method [32,33]. The generalized gradient approximation of Perdew–Burke–Ernzerhof (PBE) [34] was used for the exchange–correlation functional. The **k**-space integrations were performed with the Methfessel-Paxton method of second order [35] with a smearing width of 0.2 meV. For Mn $3p$, $3d$ and $4s$ were considered as valence electrons. $4d$, $5s$, $5p$ in case of Sn and $3d$, $4s$ in case of Zn. Lastly, for C $2p$ electrons were considered valent. The relaxation was performed for a $2 \times 2 \times 2$ supercell consisting of 24 atoms, by integration of the Brillouin zone on a gamma-centred **k**-grid with a $3 \times 3 \times 3$ mesh for a force convergence of 0.1 meV/Å. To calculate DOS, the integration of the Brillouin zone was performed utilizing the tetrahedron method with Blöchl corrections with a $9 \times 9 \times 9$ grid. The plane-wave cut-off energy for all calculations was set at 520 eV.

3. Results and discussion

3.1. Structural properties

The X-Ray diffraction (XRD) patterns of the $Mn_3Sn_{1-x}Zn_xC$ compounds measured at 298 K are shown in Fig. 1a. The Rietveld refinement of the measured patterns revealed formation (> 90 wt%) of the cubic antiperovskite type $Pm-3m$ structure (space group 221) accompanied by minor impurity phases of C, MnO and $MnSn_2$. As presented in Fig. 1b, the lattice parameter *a* and the distance between the nearest Mn atoms $\left(d_{Mn-Mn} = \frac{\sqrt{2}}{2}a\right)$ decrease linearly with increasing Zn content as the covalent radius of Zn (1.22 Å) is significantly smaller in size compared to Sn (1.39 Å), which also confirms the substitutional effect of Zn-doping. As suggested by Guillaud [36], for various Mn–based compounds (e.g. MnBi, MnSb, MnAs), the lowest distance between nearest Mn atoms giving rise to positive (FM) exchange interactions was experimentally estimated to be about 2.81 Å. Therefore, a Mn-Mn distance below 2.81 Å should correspond to negative (AFM or FiM) interactions. In the studied system, positive interactions between Mn atoms at room temperature occur for $x \geq 0.5$, thus for a Mn-Mn distance of 2.79 to 2.77 Å. Despite the preserved cubic lattice structure, confirmed by XRD analysis, local distortions of the Mn_6C octahedra can lead to deviations in the Mn-Mn distance. To confirm the presence of local distortions further research is needed employing other instrumental techniques, e.g. EXAFS [23,37]. Alternatively, the critical distance of 2.72 Å, empirically estimated for Mn_4N, can be more adequate for the $Mn_3Sn_{1-x}Zn_xC$ system, as also suggested by Li and co-workers [12]. The experimental value of the Mn-Mn distance is determined for alloys, in which magnetic order is considered in terms of direct exchange interactions. Previous studies suggested the presence of different mechanisms in antiperovskites, such as the Ruderman-Kittel-Kasuya-Yosida (RKKY) interactions [38,39].
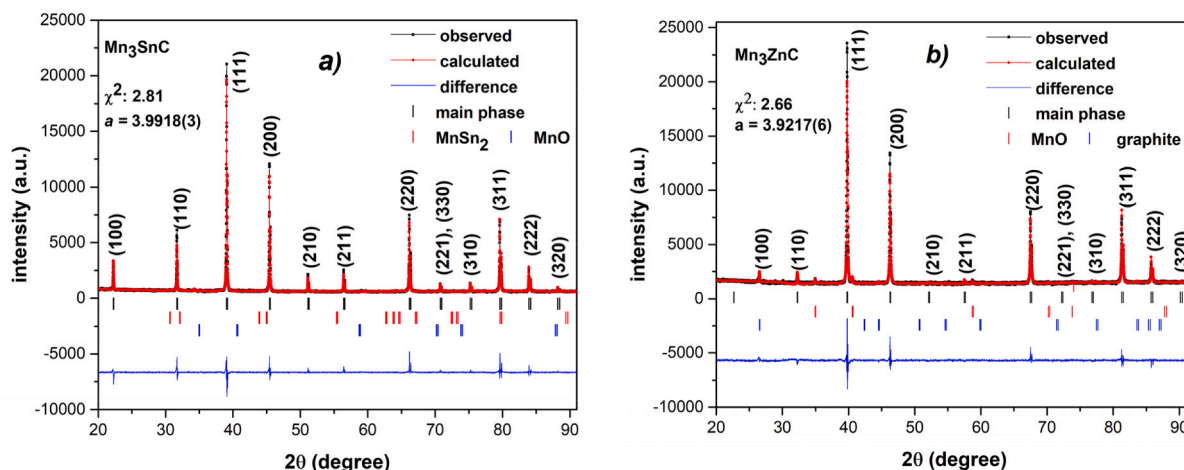
Fig. 2. Observed and calculated XRD patterns of a) Mn_3SnC and b) Mn_3ZnC at 298 K.
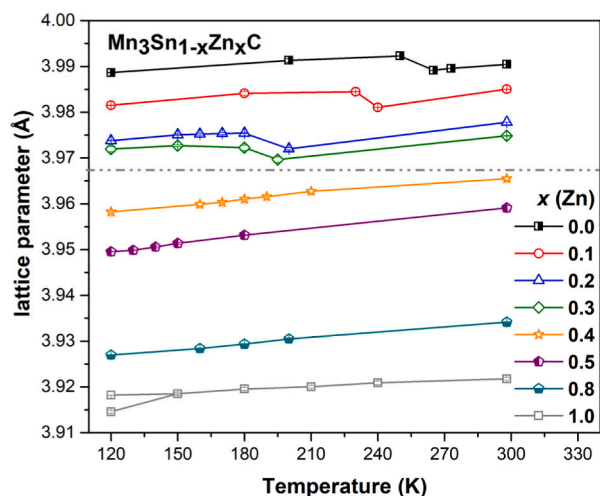

Fig. 3. Temperature dependence of lattice parameter a for $Mn_3Sn_{1-x}Zn_xC$ obtained from the XRD measurements. The error bars are smaller than the size of the marker.

Unlike the previously mentioned Mn-based compounds, Mn_4N crystallizes in the antiperovskite type of structure and shows a ferrimagnetic behaviour, which can lead to a better match of the experimentally

estimated critical distance between Mn atoms. The refinements of the XRD data collected at 298 K for $x = 0.0$ and $x = 1.0$ are shown in Fig. 2a and Fig. 2b.

The temperature dependence of the lattice parameter obtained for $Mn_3Sn_{1-x}Zn_xC$ in the temperature range 120 to 298 K is shown in Fig. 3. As observed for a Zn content in the range $0.0 \leq x \leq 0.3$, the magnetic transition is accompanied by a discontinuous jump in the lattice parameter without a change in crystal symmetry, which suggests that the FiM-PM transition is of first order. The values of $\Delta a/a$ at the transition are 0.09, 0.09, 0.08, 0.07 %, for $x = 0.0, 0.1, 0.2, 0.3$, respectively. In the vicinity of the magnetic transition, a coexistence of two phases with the same cubic symmetry, but with slightly different lattice parameters, can be seen. The temperature evolution of the (2 0 0) diffraction peak across the magnetic transition for $x = 0.1$ is depicted in **Fig. S1** in the Supplementary Material. This gradual decrease in $\Delta a/a$ suggests a suppression of the FOMT and a shift towards a SOMT. It can be noticed that for $x = 1.0$ measured at 120 K, a splitting in the lattice parameter can be seen, which reveals a distortion of the high-symmetry cubic phase towards the tetragonal $P4/mmm$ structure (space group 123) with lattice parameters $a = b = 3.9191(3)$ Å and $c = 3.9149(4)$ Å. The low-temperature XRD pattern of Mn_3ZnC is shown in **Fig. S2** (Supplementary Material). The distortion towards the tetragonal structure occurring in Mn_3ZnC can theoretically be deduced using the Goldschmidt tolerance factor (τ), which describes the stability of the antiperovskite lattice structure based on the ionic radii of the atoms:

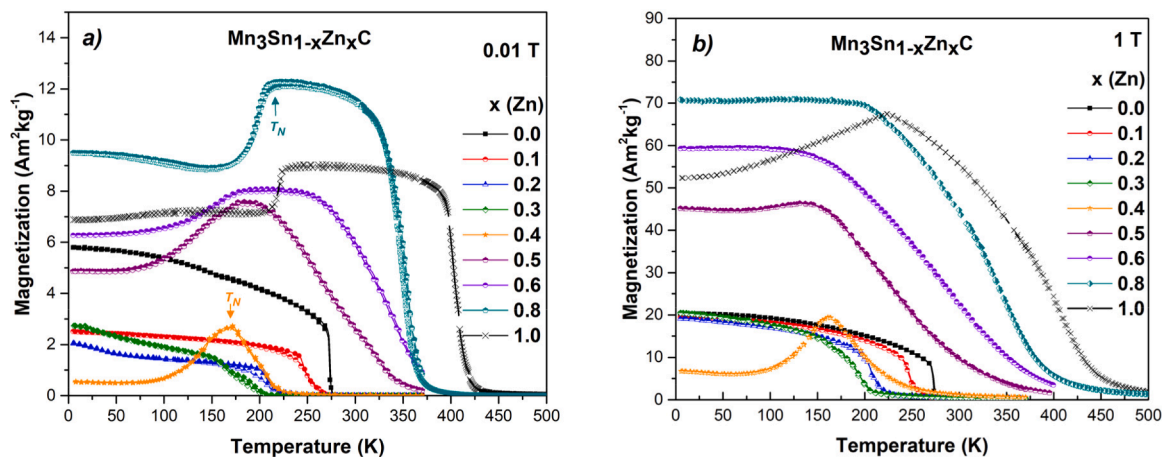**Fig. 4.** Temperature dependence of the magnetization of $Mn_3Sn_{1-x}Zn_xC$ compounds measured in a magnetic field of a) 0.01 T, b) 1 T. The systematic error in magnetization δM is 0.5 % or less, the systematic error in the temperature δT = 0.1 + 0.001 T K or less [48].
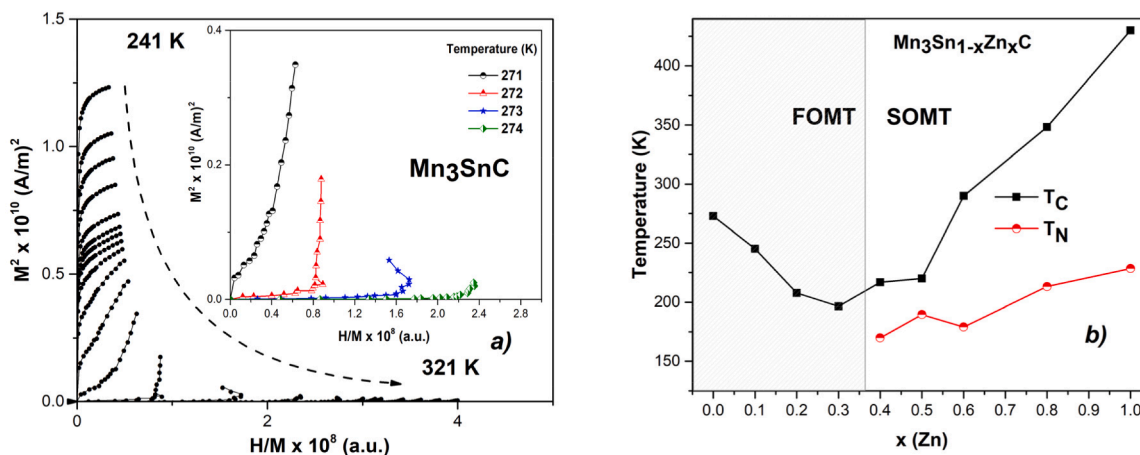
Fig. 5. a) Arrott plots derived for Mn$_3$SnC from isofield curves measured upon heating in the vicinity of T_C, b) changes in T_C and T_N as a function of Zn content in Mn$_3$Sn$_{1-x}$Zn$_x$C compounds. The error bars for T_C and T_N are within the marker size (± 1 K).

$$\tau = \frac{r_{Sn/Zn} + r_{Mn}}{\sqrt{2}(r_C + r_{Mn})} \qquad (1)$$

The structure of the highest (cubic) symmetry is stable when the Mn-C and Zn/Sn-C bonds are well-matched, which results in one degree of freedom and $\tau = 1.00$. However, in real systems, the cubic structure is adopted for compounds with $\tau = 0.91$ to 1.00 and a decrease in the Goldschmidt tolerance factor results in the formation of lower symmetry structures [40]. Due to the presence of metallic and covalent bonds in antiperovskites, the tolerance factor rarely provides precise information. Nevertheless, it can be noted that in comparison to Mn$_3$SnC ($\tau = 1.03$), the Goldschmidt tolerance factor for Mn$_3$ZnC is significantly lowered ($\tau = 0.97$) towards the tetragonal structure ($\tau = 0.71 - 0.90$), which also explains the distortion of the cubic structure.

3.2. Magnetic and magnetocaloric properties

The temperature dependence of the magnetization measured at 0.01 and 1 T are shown in Fig. 4a and Fig. 4b, respectively. The parent compound – Mn$_3$SnC, exhibits a sharp FiM-PM transition with $T_C = 273$ K, which is in good agreement with previous reports [12,21,25,41–43]. The characteristic *S*-shape of the Arrott plots in the vicinity of T_C (Fig. 5a) is indicative of the FOMT. It can be noticed that samples of x (Zn) < 0.4 all show similar magnetic behaviour. Namely, the FiM-PM transition is observed upon increasing temperature. As evidenced by the thermal hysteresis in the external magnetic field of 0.01 T, these compounds undergo a FOMT, which is also in agreement with a discontinuous change of the lattice parameter reported in section 3.1. The compound with $x = 0.4$ shows a significant change in magnetic behaviour. It can be seen that the magnetization gradually increases with increasing temperature, reaching its maximum at 170 K, which corresponds to the Néel temperature (T_N), defined by the maximum of magnetization derived from $M-T$ curves at 0.01 T, as shown in Fig. 4a. The Curie temperature is determined by the maximum from the derivative of the temperature dependence of the magnetization ($|dM/dT|$) measured at 0.01 T. Since magnetization does not approach zero at low temperatures, T_N is most likely ascribed to a FiM-FM transition, followed by a FM-PM transition upon heating, with $T_C = 217$ K. The changes in T_C and T_N in the Mn$_3$Sn$_{1-x}$Zn$_x$C system are presented in Fig. 5b. The magnetic behaviour of the Mn$_3$Sn$_{1-x}$Zn$_x$C compounds with $x \geq 0.4$ resembles Mn$_3$ZnC, for which two subsequent transitions can be observed. Recent studies revealed the influence of the packing fraction on the local distortions of the Mn$_6$C octahedra, leading to long and short Mn-Mn distances, while the cubic structure remains unaltered [23,44,45]. With increasing Zn content, the packing fraction decreases, which results in more space for the distortion of the Mn$_6$C octahedra. Consequently,
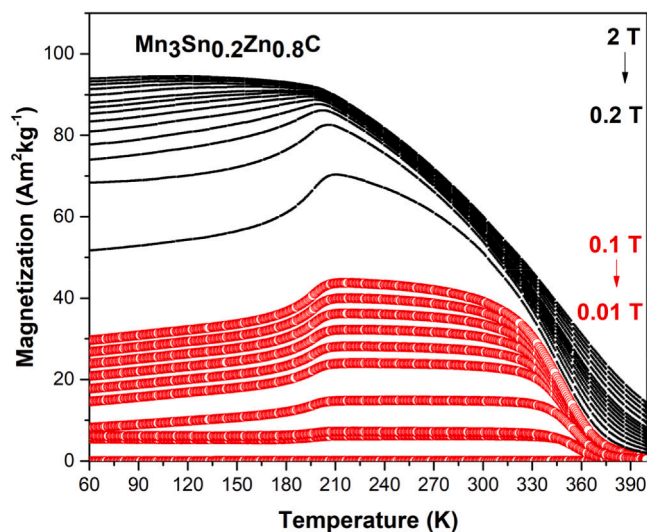

Fig. 6. Temperature dependence of the magnetization measured for x (Zn) $= 0.8$ in magnetic fields up to 2 T.

pronounced changes in magnetic behaviour can be observed due to the variation in the long and short Mn-Mn distances, aiding FM and AFM interactions, respectively. Additionally, in alloys of a higher Zn content ($x > 0.3$), a characteristic broadening of the magnetization curve can be observed at low magnetic fields. This broadened transition smears out when higher magnetic fields ($\mu_0 H > 0.2$ T) are applied, as depicted in Fig. 6 for $x = 0.8$. In these compounds, the span of the magnetic phases broadens significantly upon increasing Zn content, which suggests competing FM-AFM interactions, as previously observed in Mn$_{1-x}$Fe$_x$SnC [46] and Mn$_3$Ga$_{1-x}$Sn$_x$C [47].

The field dependence of the magnetization measured at 5 K and in magnetic fields up to 5 T revealed a significant increase in magnetization from 21.82(4) to 76.2(2) Am^{2}kg^{-1} for a change in Zn content from $x = 0.0$ to 0.8, as presented in Fig. 7a. The magnetic isotherms measured at 5 K reveal the presence of magnetic hysteresis in the compounds with $x > 0.3$, which can be ascribed to the existence of the FiM ordering. The field-dependent magnetization for x (Zn) $= 0.4$ shows an initial rise, followed by a linear increase in magnetization for higher magnetic fields (Fig. 7b). It is apparent that the magnetization does not saturate in the maximum applied magnetic field of 5 T, which in combination with accompanying magnetic hysteresis suggests the presence of a low-–temperature FiM state.
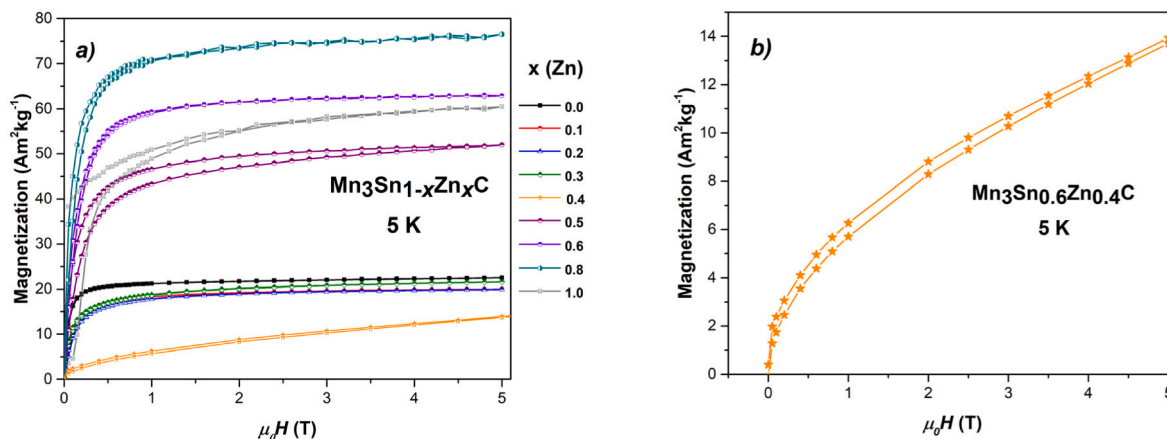
Fig. 7. a) Field dependence of magnetization for $Mn_3Sn_{1-x}Zn_xC$ compounds measured at 5 K, b) field dependence of the magnetisation for the compound with *x* (Zn) = 0.4 measured at 5 K. The systematic error in magnetization δM is < 0.5 %, the systematic error in the magnetic field δH is < 0.1 % [48].
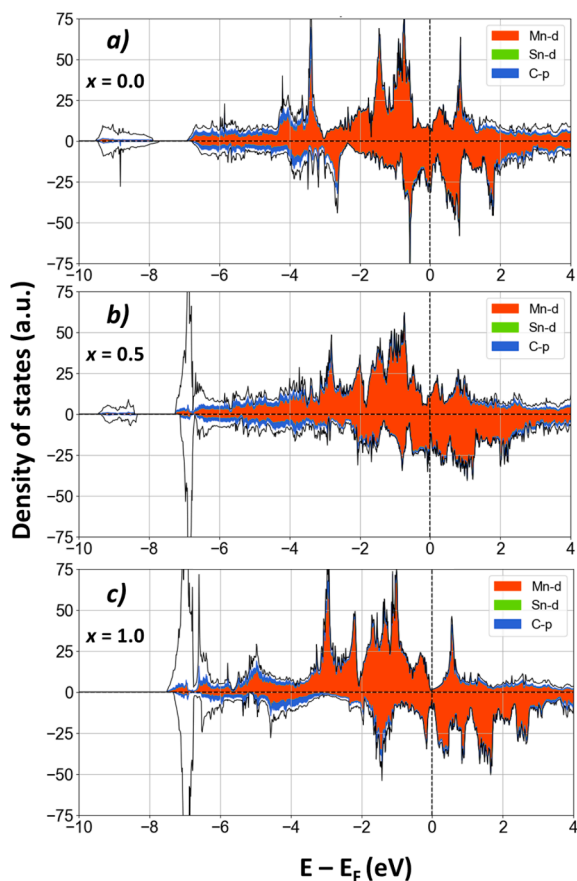

Fig. 8. DOS of $Mn_3Sn_{1-x}Zn_xC$ in the vicinity of Fermi level (E_F) for: a) *x* = 0.0, b) *x* = 0.5 and c) *x* = 1.0.

Fig. 9. Magnetic entropy change ($-\Delta S_m$) of $Mn_3Sn_{1-x}Zn_xC$, derived from $M-T$ curves measured in a magnetic field change of 2 T.

In Mn-based antiperovskites, the magnetic coupling through Mn-*X*-Mn channels competes with the direct interactions between Mn atoms [49,50]. We argue that Zn doping initially suppresses the exchange interactions between Mn atoms due to enhanced C-*2p* Mn-*3d* hybridization, which subsequently results in a decrease in T_C, as observed for *x* < 0.3. The enhanced hybridization can be seen as the overlap of the energy range for C-*2p* and Mn-*3d* orbitals in the density of states (DOS) plots presented in Fig. 8a-c. However, when *x* ≥ 0.4, then the direct exchange between Mn atoms is strongly enhanced, which leads to an abrupt increase in T_C. This phenomenon seems to be universal in many Mn-based
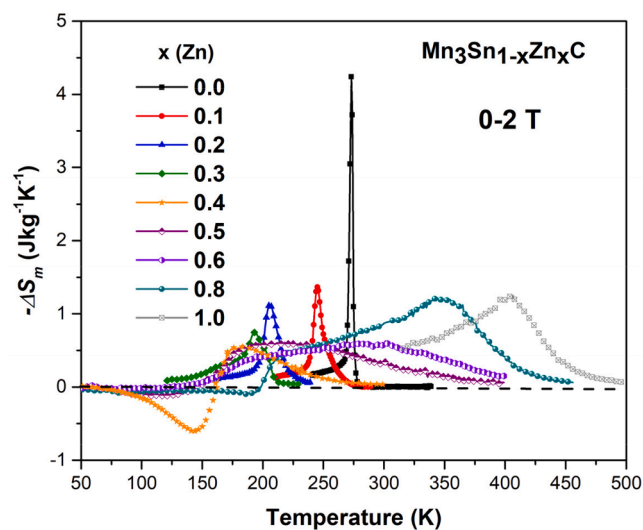
antiperovskites since a similar initial decrease in T_C followed by an increase for a higher doping content was previously observed in structurally similar compounds: $Mn_{3+x}Sn_{1-x}C$ [12,41], $Mn_3Ga_{1-x}Sn_xC$ [47], $Mn_3Sn_{1-x}In_xC$ [45], $Mn_3Sn_{1-x}Si_xC$ and $Mn_{3-x}Fe_xSnC$ [46].

According to our DFT calculations, Mn-*3d* electrons mainly contribute to the DOS at the Fermi level (E_F). As seen for the parent compound (Mn_3SnC) in Fig. 8a, a sharp peak of DOS is located at E_F, which implies a strong dependence of structural and magnetic properties upon altering the number of conduction electrons. As a result, changes in magnetic behaviour are expected upon doping, which agrees with magnetization results discussed earlier. Due to the enhanced hybridization between C-*2p* Mn-*3d* states, the width of the bands increases. Consequently, it can be seen in Fig. 8b that the population of the majority and the minority spins becomes equalized, which suppresses the spin polarization and results in a decrease in the magnetic moment, as experimentally observed for *x* = 0.4. In Fig. 8c, presenting *x* = 1.0, an opposite behaviour of the majority and minority spins is noticeable, which reflects enhanced magnetization, in agreement with our observations for *x* > 0.4. Therefore, the results from DFT calculations are consistent with the earlier discussed magnetic properties.

The magnetic entropy change $|\Delta S_m|$ was calculated from the $M-T$ curves in applied magnetic fields up to 2 T using one of the Maxwell relations:

Table 1
Collected values of the Curie temperature (T_C), the Néel temperature (T_N,), the magnetic entropy change ($-\Delta S_m$) and the magnetic moment per formula unit (μ) derived from the SQUID measurements at 5 K and in a maximum applied magnetic field of 5 T.

x (Zn)	T_C (K)	T_N (K)	$-\Delta S_m$ (Jkg^{-1}K^{-1})		μ (μ_B/f.u.)
			1 T	**2 T**	
0.0	273(1)	–	2.14(4)	4.24(8)	1.17(2)
0.1	245(1)	–	0.63(1)	1.36(3)	1.04(2)
0.2	208(1)	–	0.53(1)	1.13(2)	1.02(2)
0.3	197(1)	–	0.35(1)	0.75(2)	1.08(2)
0.4	217(1)	170(1)	0.27(1)	0.55(1)	0.68(1)
0.5	220(1)	190(1)	0.31(1)	0.59(1)	2.50(5)
0.6	290(1)	179(1)	0.29(1)	0.60(1)	2.97(6)
0.8	348(1)	213(1)	0.65(2)	1.22(3)	3.46(7)
1.0	430(1)	229(1)	0.71(1)	1.25(3)	2.62(5)

$$\Delta S_m(T, H) = \int_{\mu_0 H_1}^{\mu_0 H_2} \left(\frac{\partial M(T)}{\partial T} \right)_H d(\mu_0 H) \qquad (2)$$

As shown in Fig. 9, the values of $|\Delta S_m|$ decrease rapidly upon doping, while the peaks broaden significantly. It is notable that the change in $|\Delta S_m|$ is related to the relative change in the lattice parameter $|\Delta a/a|$ at the magnetic transition, as observed for compounds of $x < 0.4$. As proposed by Gschneidner and co-workers [51], the larger the volume change at the transition, the larger the structural entropy change, and thus, the total entropy change. A correlated decrease in $|\Delta S_m|$ and $|\Delta a/a|$ upon increasing Zn doping indicates the magneto-elastic nature of the transition. However, it can be noticed that $|\Delta S_m|$ decreases rapidly for a low dopant content ($x = 0.1$), whereas the volume change at the transition is comparable to the parent compound. As proposed for Mn$_3$SnC, a large MCE is associated with a reconstruction of the Fermi surface in the vicinity of the magnetic transition [22]. Therefore, it is suggested that doping suppresses the reconstruction of the electronic structure and leads to a decrease in MCE. The significance of the electronic entropy in antiperovskites and its correlation to the FOMT has been studied in detail [52]. The change in charge transfer upon Zn doping awaits detailed clarification using X-ray magnetic circular dichroism [53] or X-ray absorption near-edge structure measurements [45,54]. Our results highlight a strong correlation between various degrees of freedom, which results in a strong sensitivity to minor changes in chemical composition. The values of $|\Delta S_m|$, T_C and total magnetic moment (per formula unit) derived from magnetization measurements are presented in Table 1. The presence of the inverse MCE can be seen for higher Zn contents ($x \geq 0.4$). However, this effect remains significant only for $x = 0.4$, showing a value of $-0.61(1)$ Jkg^{-1}K^{-1}. The value of $|\Delta S_m|$ obtained experimentally for Mn$_3$SnC is in good agreement with experimental results reported by Cakir and co-workers [21] and Monte Carlo simulations performed recently by Benhouria and co-workers [26]. Despite a good agreement for Mn$_3$SnC, an expected increase in $|\Delta S_m|$ upon increasing Zn content was not observed in our study.

3.3. Neutron diffraction results

In order to obtain a better understanding of the magnetic structure and the magnetic response of prepared compounds, three alloys with a different Zn content ($x = 0.3, 0.4, 0.6$) have been selected and measured using neutron powder diffraction (NPD). As reported in Section 3.2, the selected samples show a distinctly different magnetic behaviour, despite the relatively small variation in composition. Although the crystal structure of Mn$_3$Sn$_{1-x}$Zn$_x$C remains cubic in the whole temperature range, the Mn moments in the magnetic unit cell, generated using the propagation vector $\mathbf{k} = (\frac{1}{2}, \frac{1}{2}, 0)$, are of two different types. As reported for the parent compound, two Mn atoms in the square configuration (*a-b* plane) carry a large AFM moment ($\mu_1 = 2.3$ μ_B/Mn) and one Mn atom has
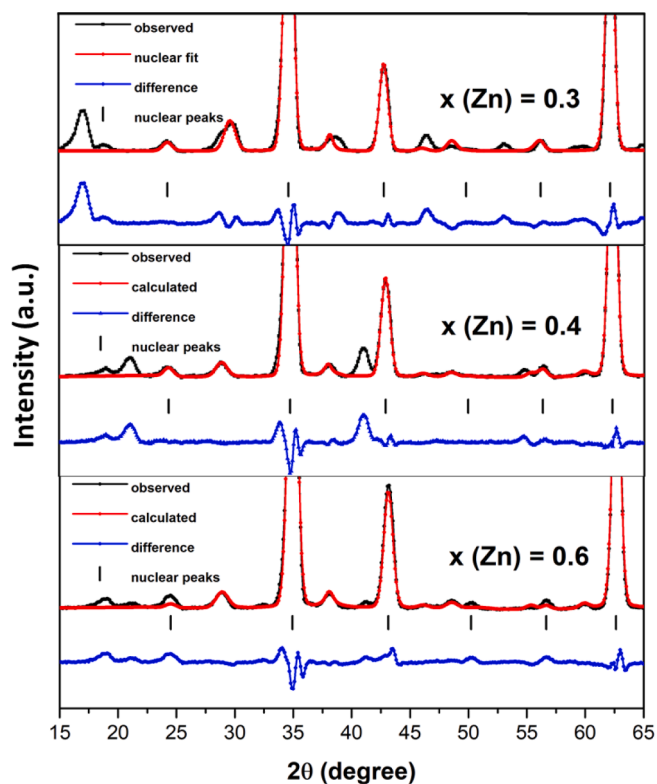

Fig. 10. Neutron diffraction patterns at 100 K with a fit of only the nuclear contribution.

a smaller FM component ($\mu_2 = 0.7$ μ_B/Mn) along the *c*-axis [37,55]. The neutron diffraction patterns at 100 K with fits that only include the contribution of the nuclear structure are shown in Fig. 10. For clarity, the nuclear fit includes the main and secondary phases, but the peaks marked in the refinement refer only to the main phase. As a result, the position and intensity of magnetic peaks can be derived from the difference between the observed intensity and the nuclear fit (blue line). Although the nuclear structure is similar in each case, the magnetic structure of these three alloys is expected to be distinctly different, judging from the pronounced differences in magnetic contribution to the patterns. The fits of both the nuclear and magnetic contributions are shown in Fig. 11a-c. The magnetic peak present at $2\theta = 18.9°$ in all patterns corresponds to the AFM magnetic phase of MnO (being magnetic below $T_N = 117$ K) and is therefore not included in the refinement.

The refinement of the neutron powder diffraction patterns in the PM state was used to elucidate site occupancies. The atoms of Sn/Zn, Mn and C were placed at the *1a* (0,0,0), *3c* (0,1/2,1/2) and *1b* (1/2,1/2,1/2) sites, respectively. The Rietveld refinement of the occupancies revealed a slight deficiency of corner sites that mainly pertains to Sn atoms. As a result, the refined compositions can be denoted as: Mn$_{3.05}$Sn$_{0.65}$Zn$_{0.30}$C$_{1.00}$, Mn$_{3.00}$Sn$_{0.55}$Zn$_{0.40}$C$_{1.05}$, Mn$_{3.10}$Sn$_{0.30}$Zn$_{0.55}$C$_{1.05}$, for the nominal Zn content $x = 0.3, 0.4, 0.6$, respectively. These Sn/Zn deficient and Mn-rich compositions might indicate partial occupancy of the *1a* site by Mn atoms, which can result in additional Mn-Mn interactions. Since a similar magnetic behaviour was observed in earlier studies [12,45,56], we claim that this minor occupancy of *1a* site by Mn is not responsible for the changes observed in the magnetic structure of the compounds studied here.

The magnetic structure of $x = 0.3$ is described with a propagation vector $\mathbf{k} = (\frac{1}{2}, \frac{1}{2}, 0)$, which indicates that the magnetic unit cell becomes doubled in both the *a* and *b* directions. The magnetic spin alignment of the Mn moments, obtained from the neutron data collected at 100 K is presented in Fig. 12a. Similar to the parent compound, the magnetic moments of the two Mn atoms form a canted AFM square arrangement (μ_1), whereas one Mn moment shows FM order (μ_2) along the *c* axis and
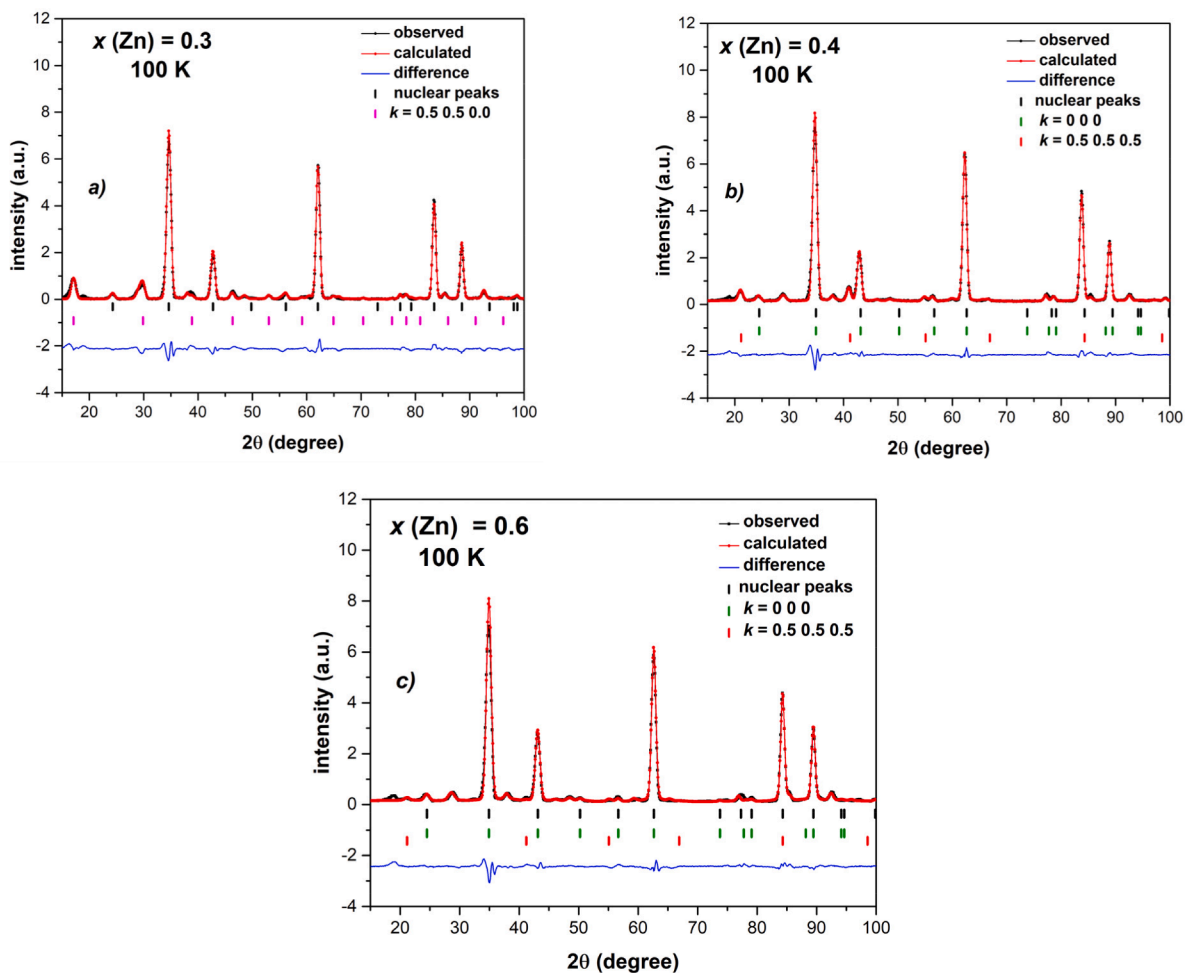
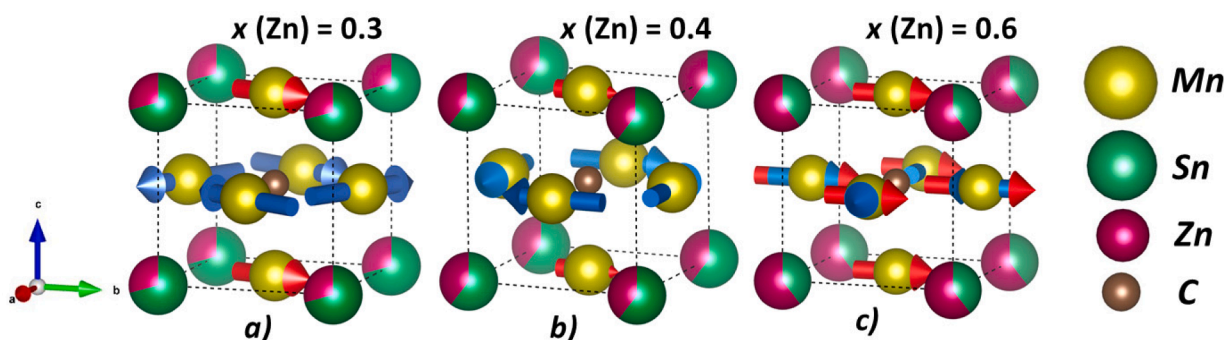**Fig. 11.** Neutron diffraction patterns at 100 K with a fit of both the nuclear and magnetic contributions.

Fig. 12. Magnetic spin alignment of the Mn moments in a nuclear unit cell structure obtained from NPD at 100 K for a) x (Zn) = 0.3, b) x (Zn) = 0.4, c) x (Zn) = 0.6. The partial occupancies represent the aimed compositions. The blue and red vectors indicate the AFM and FM moments, respectively.

aligns in the a-b plane. The FM order is described by propagation vector $\mathbf{k}$ = (0,0,0). Although the magnetic structure is similar to Mn_3SnC, the magnitude of the μ_1 magnetic moment decreases to 1.6(2) μ_B/Mn and the μ_2 moment increases to 1.03(4) μ_B/Mn, at the lowest measured temperature of 4 K. The Curie-Weiss fit to the paramagnetic susceptibility yielded an effective moment of 4.2 μ_B/f.u, calculated as $\mu_{eff} = \sqrt{8C}\,\mu_B$ where C is the Curie constant derived from the inverse susceptibility χ^{-1} as a function of temperature. The positive value of the Curie-Weiss temperature (θ_{CW} = 115.3 K) confirms the presence of FM interactions in this compound. The plots of the inverse susceptibility as a function of the temperature can be found in the Supplementary Material

(Fig. S3). The attained value of the effective moment is in agreement with the total magnetic moment of 4.2(3) μ_B/f.u obtained from neutron diffraction results at 4 K. In spite of the expected increase in $|\Delta S_m|$ due to a reduction of the AFM component [21], in our study we observe an opposite effect. According to previous studies on antiperovskites: $Mn_3Cu_{1-x}Ge_xN$ [57,58], $Mn_3Sn_{1-x}Si_xC_y$ [56] and Mn_3NiN [59], the AFM spin arrangement obtained with a propagation vector $\mathbf{k}$ = (½,½,0) is responsible for the presence of the magneto-volume effect (MVE). In our study, this finding is supported by the alleviation of the AFM component upon doping, accompanied by a reduction of $\Delta a/a$, as shown in Section 3.1. As a result, a decrease in the AFM component contributes to a
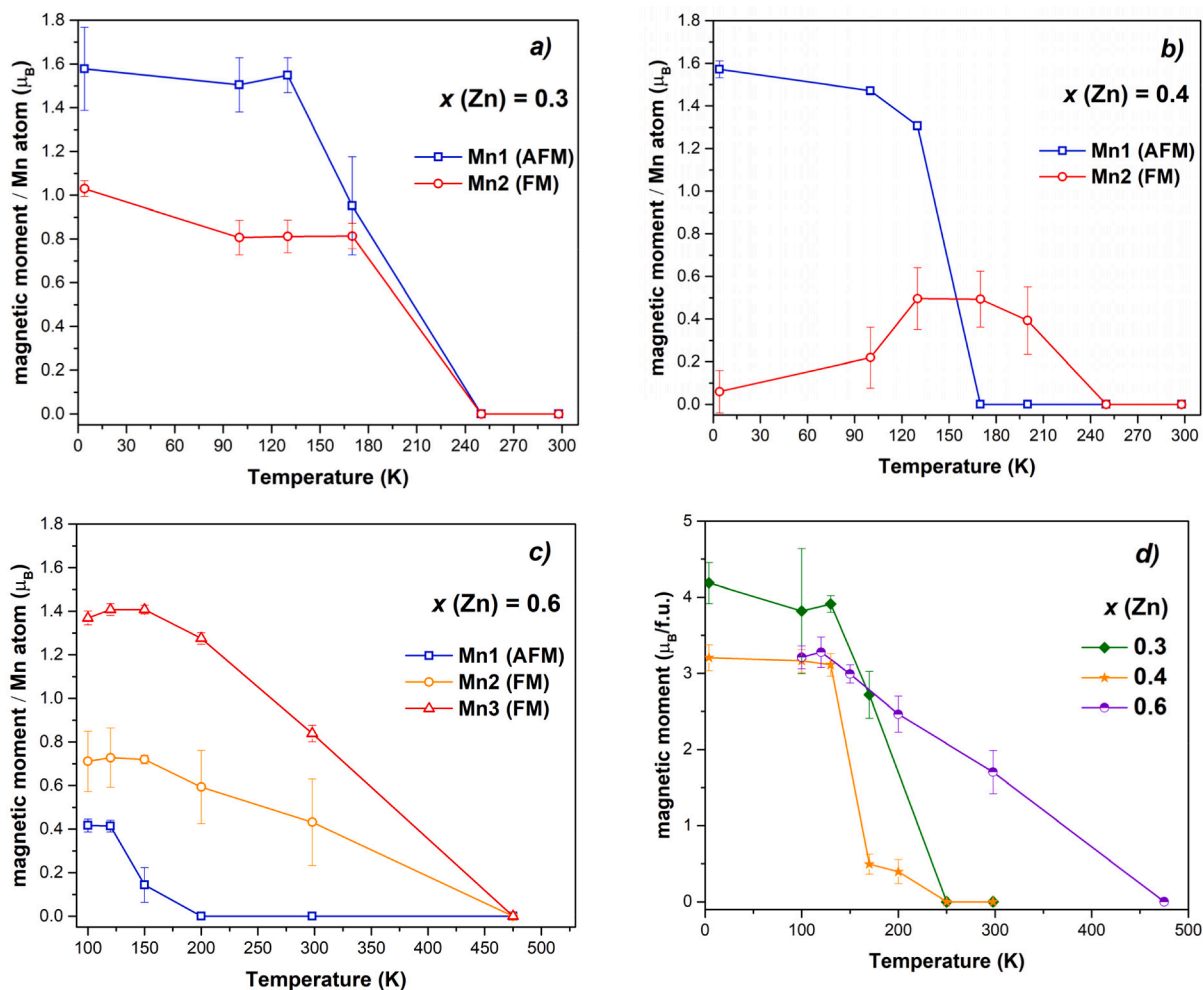
Fig. 13. Temperature evolution of magnetic moments in $Mn_3Sn_{1-x}Zn_xC$ for a) $x = 0.3$, b) $x = 0.4$, c) $x = 0.6$ obtained from NPD. d) Temperature evolution of the total magnetic moment for $x = 0.3$, 0.4, 0.6.

reduction of $|\Delta S_m|$ due to a weakening of the magnetoelastic nature of the transition. The correlation between the MVE and AFM spin arrangement relates to a geometrical corner-sharing-type frustration that occurs due to the octahedral arrangement of the Mn atoms. It is worth mentioning that a broader shape of magnetic peaks at low scattering angles might indicate the presence of an incommensurate magnetic structure, which would imply the existence of frustrated Mn_6C octahedra. The use of an incommensurate propagation vector $\mathbf{k} = (0.49, 0.49, 0.02)$ yielded a slight improvement to the fit. The AFM spin arrangement obtained using an incommensurate propagation vector and the corresponding refinement of the NPD pattern measured at 100 K is shown in **Fig. S4** in the Supplementary Material.

The magnetic reflections of $x = 0.4$ are distinctly different compared to the previously presented $x = 0.3$, and can be fitted using the AFM propagation vector $\mathbf{k} = (\frac{1}{2}, \frac{1}{2}, \frac{1}{2})$, which indicates that magnetic structure doubles in the a, b and c directions with respect to the nuclear unit cell. The observed change in magnetic structure agrees well with a notable change in magnetic properties discussed in section 3.2. As evidenced from the refinement of the neutron diffraction data at 4 K, two Mn atoms in the a-b plane possess a large AFM moment (μ_1) with a refined size of 1.57(4) μ_B/Mn. The use of an additional propagation vector $\mathbf{k} = (0,0,0)$ revealed the presence of a minor FM moment (μ_2) on the third Mn atom. The FM moment increases with temperature and reaches the maximum value of 0.5(1) μ_B/Mn at 130 K. Therefore, the total magnetic moment of 3.2(2) μ_B/f.u obtained from the NPD at 4 K is predominantly ascribed to the AFM component. While the calculated

$\mu_{eff} = 4.8$ μ_B/f.u. is in fair agreement with the total magnetic moment obtained from the refinement of the NPD data, the value of magnetic moment derived from magnetic measurements at 5 K is remarkably lower (0.68(1) μ_B/f.u) due to the evident lack of saturation in the maximum applied magnetic field of 5 T. The spin alignment at 100 K for $x = 0.4$ is presented in Fig. 12b. The presence of a FM moment is in good agreement with the field-dependent magnetization results measured at 5 K and a positive value of the Curie-Weiss temperature ($\theta_{CW} = 210$ K) derived from the inverse susceptibility as a function of temperature.

The low-temperature neutron diffraction pattern of $x = 0.6$ was likewise fitted using two propagation vectors $\mathbf{k} = (\frac{1}{2}, \frac{1}{2}, 0)$ and $\mathbf{k} = (0,0,0)$, which confirms that FiM ordering exists below T_N, as also inferred from the macroscopic magnetization measurements and discussed in Section 3.2. With a use of a propagation vector $\mathbf{k} = (0,0,0)$ it was found that all three Mn atoms carry a FM moment along the b axis. The contribution of the FM moment can clearly be seen here as an increase in the intensity of the existing nuclear peaks. The refined FM moments are of different size: two Mn atoms have a lower FM moment of 0.6(1) μ_B/Mn, and one Mn atom carries a large FM moment of 1.2(1) μ_B/Mn, as revealed from the refinement of the data collected at 100 K. Additionally, on two Mn atoms in the a-b plane a small AFM component of 0.41(4) μ_b/Mn has been found. The FM and AFM spin alignment of $x = 0.6$, obtained from the refinement of the NPD data collected at 100 K is presented in Fig. 12c. It can be noticed that the position of peaks refined using AFM propagation vector $\mathbf{k} = (\frac{1}{2}, \frac{1}{2}, \frac{1}{2})$ is exactly the same as for $x = 0.4$, though their intensity is greatly reduced, indicating a weakening of

the AFM contribution. The total magnetic moment of 3.2(2) μ_B/f.u. determined by neutron diffraction measured at 100 K originates mainly from the FM moments, thus this value is in good agreement with the size of the magnetic moment determined from the SQUID measurement ($\mu =$ 2.97(5) μ_B/f.u.), while from the Curie-Weiss fit, the calculated effective magnetic moment of $\mu_{eff} = 4.4$ μ_B/f.u. was obtained. It can be noticed that the magnetic moment of studied compounds does not saturate in the maximal applied magnetic fields of 5 T, which explains a higher value obtained from neutron diffraction compared to the SQUID measurements.

The temperature evolution of the magnetic moments for the $x = 0.3$, 0.4, 0.6 compounds is shown in Fig. 13a-d. As presented for $x = 0.3$ (Fig. 13a), the magnitude of the AFM moment μ_1 decreases rapidly above 130 K, whereas the magnitude of the FM moment μ_2 remains almost invariant in the magnetic state. It can be seen that both moments coexist to the transition temperature and disappear in the PM state. The temperature evolution of $x = 0.4$ is presented in Fig. 13b. The AFM moment dominates at 4 K but reduces drastically upon increasing temperature. Above T_N the AFM moment vanishes entirely and only a weak FM moment exists, which also disappears above T_C. The evolution of the magnetic moment for $x = 0.6$ is depicted in Fig. 13c. It can be seen that the Mn FM moments μ_2 and μ_3 decrease steadily with increasing temperature. The decrease in the weak AFM moment is more pronounced, and above T_N only the FM moments exist. The competition between the AFM and FM components occurs from the point when the first-order magnetic transition is altered towards the second-order and can be seen as the growth of the FM moment at the expense of the AFM sublattice.

4. Conclusions

The present study reveals the impact of Zn substitution in $Mn_3Sn_{1-x}Zn_xC$ antiperovskite carbides on the structural, magnetic and magnetocaloric properties. The substitution of Zn for Sn destabilizes the cubic structure, which results in the formation of a low-temperature tetragonal structure for $x = 1.0$. An initial decrease in T_C is accompanied by suppression of the first-order magnetic transition (FOMT) and an alleviation of the magneto-volume effect (MVE) effect, which contributes to a reduction of the magnetic entropy change ($|\Delta S_m|$). An increase in T_C for higher Zn doping ($x > 0.3$) occurs along with pronounced changes in magnetic behaviour. Namely, the FiM–PM transition transforms into a FiM-FM-PM transition. Neutron powder diffraction reveals the presence of complex magnetic structures in $Mn_3Sn_{1-x}Zn_xC$ and a competition between AFM and FM interactions. The magnetic structure of x (Zn) = 0.3 is similar to the parent compound and can be described using the propagation vector $\mathbf{k} = (½,½,0)$. However, a decrease in the AFM component and an increase in the FM moment can be seen. The magnetic structure of compounds with higher Zn doping can be described using two propagation vectors $\mathbf{k} = (0,0,0)$ and $\mathbf{k} = (½,½,½)$. It was found that in the $x = 0.4$ and 0.6 compounds the AFM moment decreases and the FM moment increases upon increasing Zn doping.

CRediT authorship contribution statement

A. Kiecana: Conceptualization, Methodology, Investigation, Writing – original draft. **W. Schaefers:** Investigation, Formal analysis. **M. Thijs:** Investigation, Formal analysis. **R. Dankelman:** Investigation, Formal analysis. **H. Ojiyed:** Investigation, Formal analysis. **I. Batashev:** Investigation, Formal analysis. **F. Zhang:** Investigation, Formal analysis. **N.H. van Dijk:** Conceptualization, Supervision, Writing – review & editing. **E. Brück:** Conceptualization, Supervision, Writing – review & editing.

Declaration of Competing Interest

The authors declare that they have no known competing financial interests or personal relationships that could have appeared to influence the work reported in this paper.

Appendix A. Supplementary material

Supplementary data to this article can be found online at https://doi.org/10.1016/j.jmmm.2023.170782.

References

[1] E. Brück, "Developments in magnetocaloric refrigeration", *J. Phys. D. Appl. Phys.*, vol. 38, no. 23, 2005, doi: 10.1088/0022-3727/38/23/R01.

[2] A. Smith, C.R.H. Bahl, R. Bjork, K. Engelbrecht, K.K. Nielsen, N. Pryds, Materials challenges for high performance magnetocaloric refrigeration devices, Adv. Energy Mater. 2 (11) (2012) 1288–1318, https://doi.org/10.1002/aenm.201200167.

[3] V. Chaudhary, X. Chen, R.V. Ramanujan, Iron and manganese based magnetocaloric materials for near room temperature thermal management, Prog. Mater. Sci. 100 (2019) 64–98, https://doi.org/10.1016/j.pmatsci.2018.09.005.

[4] P. Xu, L. Hu, Z. Zhang, H. Wang, L. Li, Electronic structure, magnetic properties and magnetocaloric performance in rare earths (RE) based RE_2BaZnO_5 (RE = Gd, Dy, Ho, and Er) compounds, Acta Mater. 236 (2022) 118114, https://doi.org/10.1016/j.actamat.2022.118114.

[5] Y. Zhang, J. Zhu, S. Li, Z. Zhang, J. Wang, Z. Ren, Magnetic properties and promising magnetocaloric performances in the antiferromagnetic $GdFe_2Si_2$ compound, Sci. China Mater. 65 (5) (2022) 1345–1352, https://doi.org/10.1007/s40843-021-1967-5.

[6] D. Guo, L. M. Moreno-Ramírez, J. Law, Y. Zhang, and V. Franco, "Excellent cryogenic magnetocaloric properties in heavy rare-earth based $HRENiGa_2$ (HRE = Dy , Ho , or Er) compounds", vol. 66, no. 1, pp. 249–256, 2023.

[7] D. Guo, L.M. Moreno-Ramírez, C. Romero-Muñiz, Y. Zhang, Y. Zhang, J.-Y. Law, V. Franco, J. Wang, Z. Ren, First- and second-order phase transitions in RE_6Co_2Ga (RE = Ho, Dy or Gd) cryogenic magnetocaloric materials, Sci. China Mater. 64 (11) (2021) 2846–2857, https://doi.org/10.1007/s40843-021-1711-5.

[8] W. Wu, Z. Feng, L. Guo, Estimation on magnetic refrigeration material $(Gd_{1-x}RE_x)_5Si_4$ (RE = Dy, Ho), J. Mater. Sci. Technol. 22 (6) (2006) 839–842.

[9] Z.G. Xie, D.Y. Geng, Z.D. Zhang, Reversible room-temperature magnetocaloric effect in Mn_5PB_2, Appl. Phys. Lett. 97 (20) (2010) 2–5, https://doi.org/10.1063/1.3518064.

[10] Z. Ma, P. Xu, J. Ying, Y. Zhang, and L. Li, "Insight into the structural and magnetic properties of $RECo_{12}B_6$ (RE = Ce , Pr , Nd) compounds : A combined experimental and theoretical investigation," *Acta Mater.*, vol. 247, no. February, p. 118757, 2023, doi: 10.1016/j.actamat.2023.118757.

[11] Y. Zhang, S. Li, L. Hu, X. Wang, L. Li, M. Yan, Excellent magnetocaloric performance in the carbide compounds $RE2Cr2C3$ (RE = Er, Ho, and Dy) and their composites, Mater. Today Phys. 27 (2022) 100786, https://doi.org/10.1016/j.mtphys.2022.100786.

[12] Y.B. Li, W.F. Li, W.J. Feng, Y.Q. Zhang, Z.D. Zhang, Magnetic, transport and magnetotransport properties of $Mn_{3+x}Sn_{1-x}C$ and $Mn_3Zn_ySn_{1-y}C$ compounds, Phys. Rev. B - Condens. Matter Mater. Phys. 72 (2) (2005) 1–8, https://doi.org/10.1103/PhysRevB.72.024411.

[13] X.H. Zhang, Y. Yin, Q. Yuan, J.C. Han, Z.H. Zhang, J.K. Jian, J.G. Zhao, B. Song, Magnetoresistance reversal in antiperovskite compound $Mn_3Cu_{0.5}Zn_{0.5}N$, J. Appl. Phys. 115 (2014) 123905, https://doi.org/10.1063/1.4869797.

[14] N. Hoffmann, T.F.T. Cerqueira, J. Schmidt, M.A.L. Marques, "Superconductivity in antiperovskites", npj Comput. Mater. 8 (1) (2022) 150, https://doi.org/10.1038/s41524-022-00817-4.

[15] K. Takenaka, H. Takagi, Giant negative thermal expansion in Ge-doped antiperovskite manganese nitrides, Appl. Phys. Lett. 87 (2005) 261902, https://doi.org/10.1063/1.2147726.

[16] T. Hamada, K. Takenaka, Giant negative thermal expansion in antiperovskite manganese nitrides, J. Appl. Phys. 109 (2011), https://doi.org/10.1063/1.3540604.

[17] J. Zemen, Z. Gercsi, K. Sandeman, Piezomagnetism as a counterpart of the magnetovolume effect in magnetically frustrated Mn-based antiperovskite nitrides, Phys. Rev. B 96 (2017), https://doi.org/10.1103/PhysRevB.96.024451.

[18] P. Lukashev, R. F. Sabirianov, and K. Belashchenko, "Theory of the piezomagnetic effect in Mn-based antiperovskites", *Phys. Rev. B Condens. Matter Mater. Phys.*, vol. 78, no. 18, 2008, doi: 10.1103/PhysRevB.78.184414.

[19] D. Boldrin, E. Mendive-Tapia, J. Zemen, J.B. Staunton, T. Hansen, A. Aznar, J.-L. Tamarit, M. Barrio, P. Lloveras, J. Kim, X. Moya, L.F. Cohen, Multisite exchange-enhanced barocaloric response in Mn$_3$NiN, Phys. Rev. X 8 (4) (2018) 1–9, https://doi.org/10.1103/PhysRevX.8.041035.

[20] T. Tohei, H. Wada, T. Kanomata, Negative magnetocaloric effect at the antiferromagnetic to ferromagnetic transition of Mn$_3$GaC, J. Appl. Phys. 94 (3) (2003) 1800–1802, https://doi.org/10.1063/1.1587265.

[21] F. Çaklr, M. Cugini, K. Solzi, M.A. Priolkar, M. Farle, Dynamics of nonergodic ferromagnetic/antiferromagnetic ordering and magnetocalorics in antiperovskite Mn$_3$SnC, Phys. Rev. B 96 (1) (2017) 1–6, https://doi.org/10.1103/PhysRevB.96.014436.

[22] B.S. Wang, P. Tong, Y.P. Sun, X. Luo, X.B. Zhu, G. Li, X.D. Zhu, S.B. Zhang, Z.R. Yang, W.H. Song, J.M. Dai, Large magnetic entropy change near room temperature in antiperovskite SnCMn$_3$, Europhys. Lett. 85 (2009), https://doi.org/10.1209/0295-5075/85/47004.

[23] V.N. Gaonkar, E.T. Dias, A. Das, A.K. Nigam, K.R. Priolkar, Modulations in magnetostructural coupling in C and Sn deficient Mn$_3$SnC, J. Magn. Magn. Mater. 488 (2019), https://doi.org/10.1016/j.jmmm.2019.165357.

[24] N. Ennassiri, N. Tahiri, O. El Bounagui, H. Ez-Zahraouy, A. Benyoussef, Structural, electronic, magnetic, and magnetocaloric properties in metallic antiperovskite compound Mn$_3$GaC, Mater. Res. Bull. 98 (2017) (2018) 335–339, https://doi.org/10.1016/j.materresbull.2017.10.029.

[25] V.N. Gaonkar, E.T. Dias, A.B. Dey, R.P. Giri, A.K. Nigam, K.R. Priolkar, Role of Tin and Carbon in the magnetic interactions in Mn$_3$SnC, J. Magn. Magn. Mater. 471 (2019) (2019) 215–219, https://doi.org/10.1016/j.jmmm.2018.09.070.

[26] Y. Benhouria, M. Kibbou, N. Khossossi, J. Foshi, I. Essaoudi, A. Oubelkacem, A. Ainane, R. Ahuja, Carbides-anti-perovskites Mn$_3$(Sn, Zn)C: Potential candidates for an application in magnetic refrigeration, Phys. E Low-Dimensional Syst. Nanostruct. 124 (2020) 114317, https://doi.org/10.1016/j.physe.2020.114317.

[27] S. M. L. Teicher, I. K. Svenningsson, L. M. Schoop, and R. Seshadri, "Weyl nodes and magnetostructural instability in antiperovskite Mn$_3$ZnC", *APL Mater.*, vol. 7, no. 12, 2019, doi: 10.1063/1.5129689.

[28] J. Rodríguez-Carvajal, Recent advances in magnetic structure determination by neutron powder diffraction, Phys. B Phys. Condens. Matter 192 (1–2) (1993) 55–69, https://doi.org/10.1016/0921-4526(93)90108-I.

[29] H.M. Rietveld, A profile refinement method for nuclear and magnetic structures, J. Appl. Crystallogr. 2 (2) (1969) 65–71, https://doi.org/10.1107/s0021889869006558.

[30] G. Kresse, J. Furthmüller, Efficiency of ab-initio total energy calculations for metals and semiconductors using a plane-wave basis set, *Comput. Mater. Sc*i. 6 (1) (1996) 15–50, https://doi.org/10.1016/0927-0256(96)00008-0.

[31] G. Kresse, J. Hafner, Ab initio molecular dynamics for liquid metals, Phys. Rev. B 47 (1) (1993) 558–561, https://doi.org/10.1103/PhysRevB.47.558.

[32] P.E. Blöchl, Projector augmented-wave method, Phys. Rev. B 50 (24) (1994) 17953–17979, https://doi.org/10.1103/PhysRevB.50.17953.

[33] G. Kresse, D. Joubert, From ultrasoft pseudopotentials to the projector augmented-wave method, Phys. Rev. B 59 (3) (1999) 1758–1775, https://doi.org/10.1103/PhysRevB.59.1758.

[34] J.P. Perdew, K. Burke, M. Ernzerhof, Generalized gradient approximation made simple, Phys. Rev. Lett. 77 (18) (1996) 3865–3868, https://doi.org/10.1103/PhysRevLett.77.3865.

[35] M. Methfessel, A.T. Paxton, High-precision sampling for Brillouin-zone integration in metals, Phys. Rev. B 40 (6) (1989) 3616–3621, https://doi.org/10.1103/PhysRevB.40.3616.

[36] C.P. Guillaud, Discussion, Rev. Mod. Phys. 25 (1) (1953) 119–121, https://doi.org/10.1103/RevModPhys.25.119.

[37] E.T. Dias, K.R. Priolkar, A. Das, G. Aquilanti, Ö. Çakir, M. Acet, A.K. Nigam, "Effect of local structural distortions on magnetostructural transformation in Mn$_3$SnC", J. Phys. D. Appl. Phys. 48 (29) (2015) pp, https://doi.org/10.1088/0022-3727/48/29/295001.

[38] B.S. Wang, P. Tong, Y.P. Sun, X. Luo, X.B. Zhu, G. Li, X.D. Zhu, S.B. Zhang, Z.R. Yang, W.H. Song, Large magnetic entropy change near room temperature in antiperovskite SnCMn$_3$, Epl 85 (4) (2009) pp, https://doi.org/10.1209/0295-5075/85/47004.

[39] P. Liu, J. Peng, M. Xue, B. Wang, Magnetocaloric effect and critical behavior of the Mn-rich itinerant material Mn$_3$GaC with enhanced ferromagnetic interaction, Chinese Phys. B 29 (4) (2020) pp, https://doi.org/10.1088/1674-1056/ab7da1.

[40] Z. Li, M. Yang, J.S. Park, S.H. Wei, J.J. Berry, K. Zhu, Stabilizing perovskite structures by tuning tolerance factor: formation of Formamidinium and Cesium lead iodide solid-state alloys, Chem. Mater. 28 (1) (2016) 284–292, https://doi.org/10.1021/acs.chemmater.5b04107.

[41] B.S. Wang, W.J. Lu, S. Lin, J.C. Lin, P. Tong, B.C. Zhao, W.H. Song, Y.P. Sun, Magnetic / structural diagram, chemical composition-dependent magnetocaloric effect in self-doped antipervoskite compounds Sn$_{1-xC}$Mn3$_{+x}$ ($0 \leq x \leq 0.40$), J. Magn. Magn. Mater. 324 (2012) 773–781, https://doi.org/10.1016/j.jmmm.2011.09.014.

[42] X. Shi, Y. Wen, D. Gu, H. Hou, Y. Zhang, C. Wang, The structure, magnetism and electronic transport properties of Mn$_3$Sn$_{1-x}$Zn$_x$C ($x = 0, 0.1, 0.2, 0.3, 0.4, 0.5$), J. Alloys Compd. 739 (2018) 934–938, https://doi.org/10.1016/j.jallcom.2017.12.266.

[43] D. Huang, J. Gao, Effects of Ge substitution for Sn on the crystal structure, magnetization, and the magnetocaloric effect of Mn$_3$SnC, J. Magn. Magn. Mater. 537 (2021), 168163, https://doi.org/10.1016/j.jmmm.2021.168163.

[44] A. Mungale, K.R. Priolkar, Packing fraction related distortion of Mn$_6$C octahedra and its effect on the first order magnetic transition in Mn based antiperovskites, J. Appl. Phys. 126 (24) (2019) pp, https://doi.org/10.1063/1.5130713.

[45] V.N. Gaonkar, E.T. Dias, M.N. Vedpathak, K.R. Priolkar, Packing fraction induced phase separation in A-site doped antiperovskites, Mater. Today Commun. 33 (2022), 104459, https://doi.org/10.1016/j.mtcomm.2022.104459.

[46] M. Nie, C. Wang, Y. Wen, Y. Sun, Y. Na, L. Chu, M. Tang, Magnetic phase transitions of antiperovskite Mn$_{3-x}$Fe$_x$SnC ($0.5 \leq x \leq 1.3$), Solid State Commun. 151 (5) (2011) 377–381, https://doi.org/10.1016/j.ssc.2010.12.015.

[47] E.T. Dias, K.R. Priolkar, A.K. Nigam, Co-existence of ferromagnetic and antiferromagnetic interactions in Mn$_3$Ga$_{1-x}$Sn$_x$C, Mater. Res. Express 1 (2) (2014), 026106, https://doi.org/10.1088/2053-1591/1/2/026106.

[48] H.N. Bez, H. Yibole, A. Pathak, Y. Mudryk, V.K. Pecharsky, Journal of Magnetism and Magnetic Materials Best practices in evaluation of the magnetocaloric effect from bulk magnetization measurements, J. Magn. Magn. Mater. 458 (2018) 301–309, https://doi.org/10.1016/j.jmmm.2018.03.020.

[49] L.H. Lewis, D. Yoder, A.R. Moodenbaugh, D.A. Fischer, M.-H. Yu, Magnetism and the defect state in the magnetocaloric antiperovskite Mn$_3$GaC$_{1-\delta}$, J. Phys. Condens. Matter 18 (5) (2006) 1677–1686, https://doi.org/10.1088/0953-8984/18/5/020.

[50] L. Hua, L. Wang, L.F. Chen, First-principles investigation of Ge doping effects on the structural, electronic and magnetic properties in antiperovskite Mn$_3$CuN, J. Phys. Condens. Matter 22 (20) (2010), 206003, https://doi.org/10.1088/0953-8984/22/20/206003.

[51] K.A. Gschneidner, Y. Mudryk, V.K. Pecharsky, On the nature of the magnetocaloric effect of the first-order magnetostructural transition, Scr. Mater. 67 (6) (2012) 572–577, https://doi.org/10.1016/j.scriptamat.2011.12.042.

[52] M. Piazzi, J. Zemen, V. Basso, Ab-initio based analytical evaluation of entropy in magnetocaloric materials with first order phase transitions, Phys. Procedia 75 (2015) 1332–1344, https://doi.org/10.1016/j.phpro.2015.12.149.

[53] V.N. Antonov, B.N. Harmon, A.N. Yaresko, A.P. Shpak, Electronic structure, noncollinear magnetism, and X-ray magnetic circular dichroism in the Mn$_3$ZnC perovskite, Phys. Rev. B - Condens. Matter Mater. Phys. 75 (16) (2007) 1–7, https://doi.org/10.1103/PhysRevB.75.165114.

[54] J. Chaboy, H. Maruyama, N. Kawamura, Ab initio x-ray absorption study of Mn K-edge XANES spectra in Mn$_3$MC (M = Sn, Zn and Ga) compounds, J. Phys. Condens. Matter 19 (21) (2007) pp, https://doi.org/10.1088/0953-8984/19/21/216214.

[55] J. Yan, Y. Sun, Y. Wen, L. Chu, M. Wu, Q. Huang, C. Wang, J.W. Lynn, Y. Chen, Relationship between spin ordering, entropy, and anomalous lattice variation in Mn$_3$Sn$_{1-\varepsilon}$SiεC$_{1-\delta}$ compounds, Inorg. Chem. 53 (4) (2014) 2317–2324, https://doi.org/10.1021/ic403063t.

[56] G. Lorthioir, M. E. Fruchart, M. Nardin, P. l'Héritier, and R. Fruchart, "Etude magnetique et cristallographique de la solution solide (Zn$_{1-x}$Sn$_x$)Mn$_3$C", *Mater. Res. Bull.*, vol. 8, no. 9, pp. 1027–1034, 1973, doi: https://doi.org/10.1016/0025-5408 (73)90107-4.

[57] S. Iikubo, K. Kodama, K. Takenaka, H. Takagi, S. Shamoto, Magnetovolume effect in Mn$_3$Cu$_{1-x}$Ge$_x$N related to the magnetic structure: neutron powder diffraction measurements, Phys. Rev. B - Condens. Matter Mater. Phys. 77 (2) (2008) 3–6, https://doi.org/10.1103/PhysRevB.77.020409.

[58] S. Iikubo, K. Kodama, K. Takenaka, H. Takagi, M. Takigawa, S. Shamoto, Local lattice distortion in the giant negative thermal expansion material Mn$_3$Cu$_{1-x}$Ge$_x$N, Phys. Rev. Lett. 101 (20) (2008) 1–6, https://doi.org/10.1103/PhysRevLett.101.205901.

[59] M. Wu, C. Wang, Y. Sun, L. Chu, J. Yan, D. Chen, Q. Huang, J.W. Lynn, Magnetic structure and lattice contraction in Mn$_3$NiN, J. Appl. Phys. 114 (12) (2013) pp, https://doi.org/10.1063/1.4822023.